

Water-Induced Fabric Transitions in Olivine

Haemyeong Jung and Shun-ichiro Karato*†

The interpretation of seismic anisotropy in Earth's upper mantle has traditionally been based on the fabrics (lattice-preferred orientation) of relatively water-poor olivine. Here we show that when a large amount of water is added to olivine, the relation between flow geometry and seismic anisotropy undergoes marked changes. Some of the puzzling observations of seismic anisotropy in the upper mantle, including the anomalous anisotropy in the central Pacific and the complicated anisotropy in subduction zones, can be attributed to the enrichment of water in these regions.

Propagation of seismic waves in the upper mantle of Earth is often anisotropic. Anisotropic structures may form by deformation, and hence such structures can be used to infer the flow geometry in Earth's interior (1). The relation between flow geometry and anisotropy used in these studies is based mainly on studies of naturally deformed olivine-rich rocks in the lithosphere or on the results of experimental studies on olivine under relatively low-pressure conditions (2, 3), both of which represent fabric development under water-poor conditions (4).

Although these results obtained at water-poor conditions can explain most of the seismic anisotropy in the upper mantle (1, 3), some of the recent observations of upper-mantle anisotropy cannot easily be explained by these data. They include unique anisotropy in the upper mantle beneath Hawaii where strong $V_{SH} > V_{SV}$ ($V_{SH,SV}$: velocity of SH and SV waves) anisotropy persists down to the deep (to ~200 to 300 km) upper mantle (5, 6) and the anisotropy in the subduction zone upper mantle ("wedge" mantle) where strong trench-parallel polarization of the fast S waves is observed close to the trenches (7, 8).

These observations suggest that the conventional relation between anisotropy and flow geometry might not apply to these regions. Mineral physics studies have shown that both dislocation creep and recrystallization in olivine are affected by the presence of water (9, 10). Furthermore, the effects of water in enhancing deformation in olivine are anisotropic (10) and increase with the fugacity of water (11). On the basis of these considerations, it was suggested that the deformation fabric (lattice-preferred orientation) in olivine might be modified under water-rich conditions in the upper mantle (12). In such a

case, the geodynamic significance of seismic anisotropy will be different from that inferred from previous works. Here, we report the results of an experimental study to test this hypothesis and discuss some implications for the interpretation of seismic anisotropy.

For this purpose, an essential issue in an experimental study is to realize a high fugacity of water (13). We used simple shear deformation geometry because some components of change in the fabric of the sample cannot be detected in a high-symmetry geometry such as triaxial compression. We used a solid-medium apparatus with a sample assembly appropriate for nearly simple shear deformation. To obtain a high fugacity of water, we used a mixture of talc and brucite next to the sample.

Single crystals or polycrystalline aggregates of olivine (both from San Carlos, Arizona) were used as starting materials. A sample was sheared between two pistons at a constant rate of shear (Table 1). A thin slice of sample (~0.3 to 0.5 mm thick) was sandwiched between two pistons (made of tung-

sten or alumina) cut at 45° to the compression axis. The water content was measured in each sample with a Fourier-transform infrared spectrometer (FTIR) (14). A comparison with previous data (15) showed that most of the samples show water content consistent with chemical equilibrium. After each experiment, the sample was cut into two or three sections, and its microstructure was investigated with an optical microscope as well as a scanning and transmission electron microscope (TEM). The preferred orientation of crystallographic axes was measured on a polished sample through use of an electron back-scattered pattern technique. Orientations of about 200 to 500 grains were measured for each sample.

Shear strain and uniaxial compression strain were measured by the rotation of a strain marker and by the changes in sample thickness, respectively (16). Deformation geometry was shown to be approximately simple shear with uniaxial compression contributing less than ~10% of the total strain. The magnitude of stress was estimated primarily from dislocation densities with a scanning electron microscope (17). All of the samples that deformed under high water-fugacity conditions showed a high degree of recrystallization. The degree of recrystallization was much smaller in water-poor samples. In samples with partial recrystallization, preferred orientation was measured for recrystallized portions.

The results of preferred orientation of crystallographic axes are shown in Fig. 1. LPO (lattice-preferred orientation) in water-rich samples develops quickly, presumably due to rapid recrystallization kinetics (18). Nearly steady-state fabric is achieved at a shear strain $\gamma \sim 1$ under water-saturated conditions, and the fabric is independent of starting materials. We

Table 1. Experimental conditions and the results.

Run no.	Pressure (GPa)	Temperature (K)	Fabric type	Water content (ppm H/Si)	Shear strain (γ)	Strain rate (s^{-1})	Differential stress* (MPa)
JK8	1.9	1470	B	1200	1.00	9.5×10^{-4}	340†
JK11	2.1	1470	C	1300	1.00	9.2×10^{-5}	230
JK12	2.2	1570	C	800‡	1.00	6.9×10^{-6}	250
JK18	1.9	1470	C	1310	1.20	9.5×10^{-4}	300
JK21	2.0	1570	B	200	4.00	7.9×10^{-5}	410†
JK23	2.0	1470	C	1000	4.00	1.8×10^{-4}	180
JK24	2.0	1470	C	1100	0.75	1.4×10^{-5}	160
JK25	2.0	1470	C	450§	0.60	5.6×10^{-6}	290
JK26	1.0	1470	C	700	1.06	2.1×10^{-4}	250
JK30	1.0	1470	C	650	1.02	5.5×10^{-4}	250
JK40	1.9	1470	C	1200	0.93	3.9×10^{-4}	230
JK41	2.0	1460	C	1300	0.63	1.3×10^{-4}	160
JK43	0.5	1570	A	100	1.20	3.7×10^{-5}	260
JK45	0.9	1400	B	630	0.51	4.0×10^{-4}	460†

*Differential stress was measured from the dislocation density of the samples (except for type-B samples). †Results are from the flow law by Karato and Jung (37). Because the dislocation distribution is so heterogeneous, we estimated the stress using the flow law of olivine. ‡Water content of this sample was moderate (water content ~800 ppm H/Si) because of the melting of the mixture of talc plus brucite. §This is the minimum water content of the sample because of the water loss after long deformation experiment.

University of Minnesota, Department of Geology and Geophysics, Minneapolis, MN 55455, USA.

*To whom correspondence should be addressed. E-mail: shun-ichiro.karato@yale.edu

†Present address: Department of Geology and Geophysics, Yale University, New Haven, CT 06520, USA.

have identified several different types of fabric. In addition to the well-known fabric in which the olivine [100] axis is subparallel to the shear direction and the (010) plane is subparallel to the shear plane (type-A), we identified two new types of fabrics: type-B, in which the olivine [001] axis is subparallel to the shear direction and the (010) plane is subparallel to the shear plane; and type-C, in which the [001] axis is subparallel to the shear direction and the (100) plane is subparallel to the shear plane (Fig. 1) [another type of fabric, type-D, has also been reported (19)]. The strength of the type-B fabric is generally weaker than that of the other types. The observed fabric types vary with water content and stress (Fig. 2). Type-A dominates at low stress and low water content, type-C dominates at high water content and modest stress, and type-B dominates at high water content and/or high stress (type-D dominates at high stress and low water content).

Dislocation structures in each type of sample are shown in Fig. 3. Distribution of dislocations is highly heterogeneous in type-B samples, and a large portion of grains is dislocation free (Fig. 3B) (the fraction of dislocation-free grains increases with the increase of water content). This suggests an important role of diffusion creep in the recrystallized portions of type-B samples. In contrast, dislocation distribution is more homogeneous in type-A and type-C samples (Fig. 3, A and C). There is a marked difference in dislocation microstructures between type-A sample and type-C (or type-B) sample. Well-developed subgrain structure can be seen in type-A sample but not in type-B and type-C samples. This suggests a high mobility of grain boundaries in type-B and

type-C samples due to the presence of the water (20, 21). Dislocations in type-C samples are mostly straight (Fig. 3C), whereas dislocations in other types of samples have a more curved geometry.

These observations, combined with previous results showing that the slip along the [001] direction is selectively enhanced relative to the slip along the [100] direction by the addition of water (10), provide insights into the causes of fabric transitions found in the present study. A peak of the [001] orientation subparallel to the flow direction in type-C may correspond to the contribution from the glide of dislocations with $\mathbf{b} = [001]$ [\mathbf{b} is the Burgers vector of a dislocation (22)]. This suggests that the dominant slip systems in olivine may change by the addition of water. The cause for the transition from type-C to type-B is less clear. A sizable contribution from diffusion creep suggested by dislocation structures may contribute to this fabric, but the cause underlying the transition from type-C to type-B fabric remains to be investigated.

Seismic anisotropy corresponding to these new fabrics (type-B and type-C) was calculated and compared with that from conventional fabric (type-A). For example, the V_{SH}/V_{SV} polarization anisotropy corresponding to horizontal (vertical) shear is $V_{SH} > V_{SV}$ ($V_{SH} > V_{SV}$ for vertical shear) for water-poor conditions (type-A), but it is $V_{SV} > V_{SH}$ ($V_{SH} > V_{SV}$ for vertical shear) for water-rich and/or high-stress conditions (type-B and type-C) (23). The direction of polarization of the faster S wave is subparallel to the flow direction (in a horizontal flow) in type-A (water-poor, low-stress) and type-C (water-rich, low-

stress) fabrics (Fig. 4). However, in type-B (water-rich, high-stress), the direction of polarization of the faster S wave (in a horizontal flow) is nearly perpendicular to the flow direction, which is different from those expected from the type-A fabric (Fig. 4). Consequently, the seismic anisotropy in water-rich regions corresponding to a given flow geometry will be different from that for water-poor regions, although the difference will also depend on the magnitude of the applied stress.

Although our experimental studies have explored low to high water-fugacity conditions relevant to Earth's upper mantle (4), and although the temperatures in our experiments are similar to those in the asthenosphere, other conditions such as the magnitude of stress are quite different from those in Earth: Stress magnitudes in most of Earth's mantle are expected to be smaller than those obtained in our experiments (24). Therefore, a proper extrapolation scheme must be considered to apply our results to Earth's interior. It is difficult to clearly define such a scaling law at the present, but we can determine some of the constraints using both experimental and seismological observations. Briefly, the boundary between type-C and type-A fabric, for example, is likely to have a negative slope on the water content–stress diagram, and type-B fabric should dominate in regions of high water content and high stress (25).

Among the various fabrics found in this study, type-A fabric is most commonly observed in naturally deformed peridotites (1, 3), most of which are from depleted litho-

Fig. 1. Pole figures of crystallographic orientation of deformed olivine aggregates. The east-west direction corresponds to the shear direction, and the north (south) poles correspond to the shear-plane normal. Equal area projection to the lower hemisphere is used. The color coding refers to the density of data points (the numbers in the legend correspond to the multiples of uniform distribution). We used a half scatter width of 40°. Type-A [sample MIT-23 (39); dry, $T = 1570$ K, $P = 0.3$ GPa, $\sigma = 160$ MPa, $\gamma = 1.43$], type-B [sample JK8; water-saturated, $T = 1470$ K, $P = 1.9$ GPa, $\sigma = 340$ MPa, $\gamma = 1.0$], type-C [sample JK11; water-saturated, $T = 1470$ K, $P = 2.1$ GPa, $\sigma = 230$ MPa, $\gamma = 1.0$].

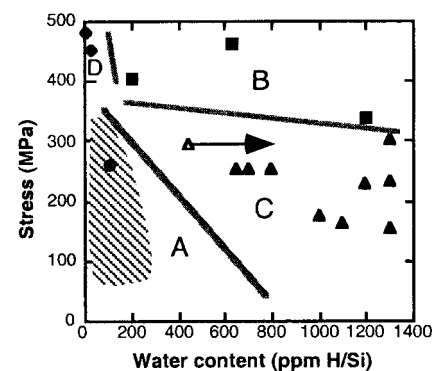
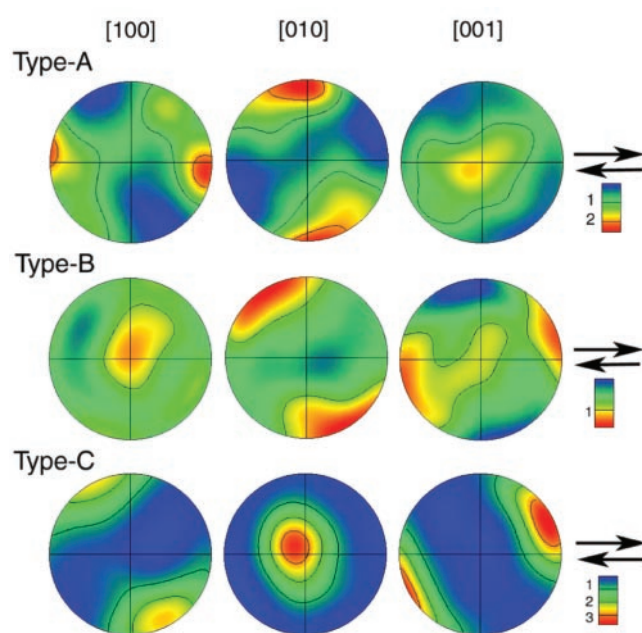


Fig. 2. A fabric diagram for olivine on a stress-water content (C_{OH}) plane at high-temperature conditions. Data shown are from the experiments at $T = 1400$ to 1570 K. The fabrics found in this study (type-A, -B, -C, and -D) are shown as a function of stress and water content (C_{OH}). Data for type-A are from this study (solid circle) and from Zhang *et al.* (39) (shaded area). Data for type-B and type-C are from this study. The open triangle indicates a data point in which a substantial amount of water has been lost during the experiment. In this case, the water content measured after the experiment is the lower bound for the actual water content during the experiment. Data for type-D are from Zhang *et al.* (39) and Bystricky *et al.* (38).

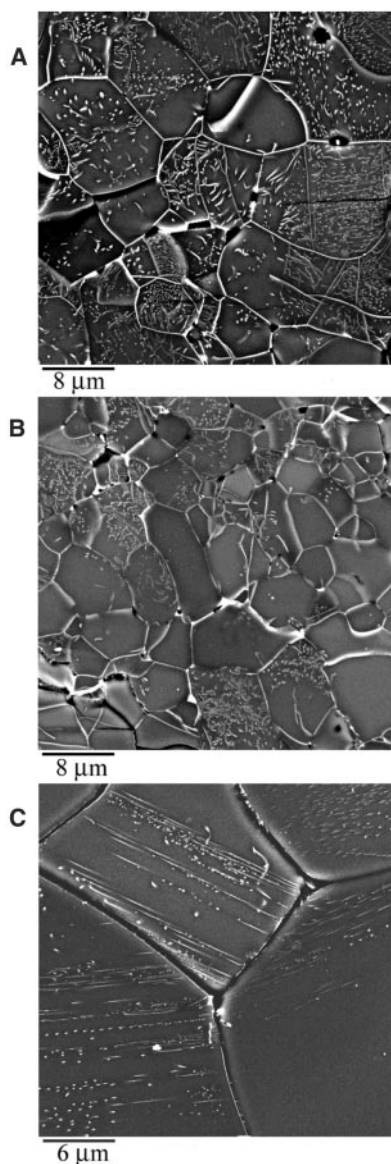


Fig. 3. Backscattered electron images of deformed samples. Bright lines show grain-boundaries or dislocations. (A) Sample JK-43 (deformed at $T = 1570$ K, $P = 0.5$ GPa, $\sigma = 260$ MPa, $\gamma = 1.2$, water-poor condition). (B) Sample JK-45 (deformed at $T = 1400$ K, $P = 0.9$ GPa, $\sigma = 460$ MPa, $\gamma = 0.5$, water-saturated condition). (C) Sample JK-11 (deformed at $T = 1470$ K, $P = 2.1$ GPa, $\sigma = 230$ MPa, $\gamma = 1.0$, water-saturated condition). Type-A and C samples have high densities of dislocations. Well-developed subboundaries are seen in the type-A sample (deformed under the "dry" condition), whereas subboundaries are rare in type-B and type-C. Overall dislocation density is low in type-B, and most dislocations in the type-C sample are straight.

sphere. This is consistent with our result showing that type-A fabric dominates under water-poor conditions. However, type-B or type-C fabric has also been documented in some naturally deformed peridotites. They include peridotites from Alpe Arami, Switzerland (26, 27); from Higashi-Akaishi-

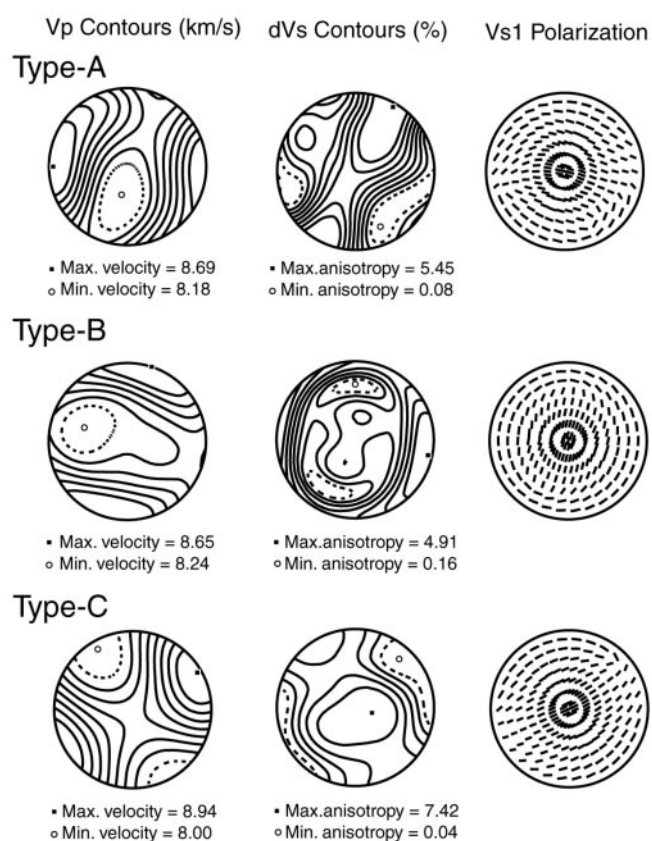


Fig. 4. Seismic anisotropy corresponding to the fabrics identified in this study (type-A: MIT-23; type-B: JK8; type-C: JK11). The east-west direction corresponds to shear direction, and the center of the plot corresponds to shear-plane normal (this coordinate is chosen to clearly illustrate the polarization directions of fast shear waves and is different from that used in Fig. 1). Azimuthal anisotropy of P waves and polarization anisotropy of S waves are shown (dVs is a contour plot of the magnitude of shear-wave polarization anisotropy and $Vs1$ is a plot of the polarization direction of fast S waves along different orientations of propagation).

Yama, Japan (28); and from Castle rock, Canada (29). All of these peridotites are considered to be from subduction zone upper mantle, where high water fugacity (and high stress) is expected. In particular, both types of fabric (type-B and type-C) are found in the peridotites from Alpe Arami and Higashi-Akaishi-Yama.

Some of the seismological observations may be attributed to the effects of high water content. For example, peculiar anisotropy in the deep upper mantle beneath Hawaii (5, 6) can be explained if the upwelling materials beneath Hawaii contain a large amount of water. Geochemical evidence for higher than normal water content in the source region of Hawaii hotspot has also been discussed (30). Anisotropy in the subduction zone upper mantle is usually attributed to complicated flow geometry (8). Although such possibilities should not be ruled out, our results offer a much simpler explanation: The polarization direction of the faster S wave near the trench is parallel to the trench because of the high water content and high stress in these environments producing the type-B fabric. In our model, the change in the direction of fast S -wave polarization reflects the change in water content (and stress), assuming a simple corner flow model. The present study provides a new dimension in the interpretation of seismic anisotropy and deformation fabric of upper-mantle peridotites. A major remaining

uncertainty is the scaling law for the fabric transitions. In particular, conditions under which type-B fabric dominates are not well constrained by the present study.

References and Notes

1. A. Nicolas, N. I. Christensen, in *Composition, Structure and Dynamics of the Lithosphere-Asthenosphere System*, K. Fuchs, C. Froidevaux, Eds. (American Geophysical Union, Washington, DC, 1987), p. 111.
2. S. Zhang, S. Karato, *Nature*, **375**, 774 (1995).
3. B. W. Ismail, D. Mainprice, *Tectonophysics*, **296**, 145 (1998).
4. Most of the peridotite samples are from the lithosphere and contain relatively low water content (31), probably due to partial melting of the samples (32, 33). Also, the recent experimental studies with a high-resolution gas-medium apparatus are made at low confining pressures (<0.5 GPa), and therefore the water content in olivine is low [~ 200 parts per million (ppm) H/Si] as compared with that in the asthenosphere [~ 800 to 3000 ppm H/Si (34)]. The higher end of this estimate corresponds to subduction zone upper mantle and the lower end to source regions of mid-oceanic ridge basalt.
5. G. Ekström, A. M. Dziewonski, *Nature*, **394**, 168 (1998).
6. J.-P. Montagner, L. Guillot, in *Problems in Geophysics for the New Millennium*, E. Boschi, G. Ekström, A. Morelli, Eds. (Editrice Compostiori, Rome, 2000), p. 217.
7. L. Margheriti, C. Nostro, M. Cocco, A. Amato, *Geophys. Res. Lett.* **23**, 2721 (1996).
8. G. P. Smith et al., *Science* **292**, 713 (2001).
9. P. N. Chopra, M. S. Paterson, *J. Geophys. Res.* **89**, 7861 (1984).
10. S. J. Mackwell, D. L. Kohlstedt, M. S. Paterson, *J. Geophys. Res.* **90**, 11319 (1985).
11. S. Mei, D. L. Kohlstedt, *J. Geophys. Res.* **105**, 21461 (2001).
12. S. Karato, *Proc. Jpn. Acad. Ser. B* **71**, 61 (1995).

13. A solid-medium high-pressure deformation apparatus such as the Griggs apparatus can be used to ~3 GPa, whereas a gas-medium high-pressure deformation apparatus such as the Paterson apparatus can be used only to ~0.5 GPa. This makes a large difference in water fugacity: ~13 GPa (at 2-GPa confining pressure and 1473 K) with a solid-medium apparatus, and ~0.6 GPa (at 0.5-GPa confining pressure and 1473 K) with a gas-medium apparatus.

14. For this purpose, a single crystal of olivine with the orientation [010] parallel to the compression axis was placed near the specimen. Absorption of the infrared beam at ~3000 to 3800 cm⁻¹ of this single crystal of olivine was measured with a FTIR spectrometer, and the calibration by Paterson (35) was used to calculate water content from the absorption coefficient.

15. D. L. Kohlstedt, H. Keppler, D. C. Rubie, *Contrib. Mineral. Petrol.* **123**, 345 (1996).

16. Rotation of a strain marker and the change in sample thickness were measured after each experiment. The shear strain, γ , was calculated from the rotation angle of a strain marker, θ , as $\gamma = \tan\theta$, and the shortening strain, ϵ , was calculated from $\epsilon = \Delta h/h$ where h is the initial sample thickness and Δh is the change in sample thickness.

17. Measurement of a stress magnitude in samples deformed by a solid-medium apparatus is not trivial. Measurements by an external load-cell have very large errors and do not provide reliable values of stress. We used high-resolution dislocation density measurements to estimate the stress magnitude (36). Values of stress in Table 1 are obtained from the measurements of dislocation densities and have uncertainties of ~±10 to 15% (21). This technique works for type-A, -C, and -D samples, but not for type-B samples in which dislocation density is highly heterogeneous. Consequently, for type-B samples, a stress estimate based on flow laws was also used. The olivine flow law under water-rich conditions determined by Karato and Jung (37) was used to estimate the magnitude of stress from known temperature, pressure, strain rate, and water fugacity.

18. The effects of dynamic recrystallization to enhance fabric development have been demonstrated by Zhang and Karato (2). Bystricky *et al.* (38) reported much more sluggish kinetics of development of LPO, which is probably due to the slow kinetics of recrystallization at low temperature (1473 K) and water-poor conditions. Their results are consistent with the results obtained by Zhang *et al.* (39).

19. Carter and Avé Lallemant (40), Bystricky *et al.* (38), and Zhang *et al.* (39) reported another type of fabric (here called type-D) in which olivine [100] forms a well-defined maximum parallel to the shear direction, but in which other orientations make a girdle.

20. S. Karato, *Tectonophysics* **168**, 255 (1989).

21. H. Jung, S. Karato, *J. Struct. Geol.* **23**, 1337 (2001).

22. Our TEM observations show approximately the same number of $\mathbf{b} = [100]$ and $\mathbf{b} = [001]$ dislocations in "dry" samples, but most of the dislocations in "wet" samples (both type-B and type-C samples) have $\mathbf{b} = [001]$ Burgers vector. The $\mathbf{b} = [001]$ dislocations are mostly straight screws, indicating a high Peierls barrier.

23. We use the method described by Montagner and Nataf (41) to calculate V_{SH}/V_{SV} anisotropy.

24. Stress magnitude in Earth's upper mantle can be estimated from the microstructures of deformed rocks. Peridotites from typical rift-zone environment or xenoliths from ocean island basalts show stress magnitudes of ~1 to 10 MPa (42), whereas peridotites from collision zones (low temperature, high strain rates) show much higher stresses (~50 to 300 MPa) (43).

25. The transition from one type of fabric to another will occur when strain rates of two different slip systems coincide. Because the strain rate is a function primarily of temperature (T), stress (σ), and water content (C_{OH}), the boundary must be a surface in a three-dimensional space (T - σ - C_{OH}) defined by a function $f(T, \sigma, C_{OH}) = K$, where K is a constant. The temperatures in our experiments are close to those in the asthenosphere, and therefore boundaries in a σ - C_{OH} plane will be a good approximation to real boundaries in the hot regions of Earth (asthenosphere). From our experiments at low water content, we know

that this boundary must pass a point $C_{OH} \cong 200$ ppm H/Si and $\sigma \cong 400$ MPa. Also, seismological observations show that the asthenosphere in a typical oceanic upper mantle [for which $C_{OH} \cong 800$ ppm H/Si (33) and $\sigma \cong 1$ to 10 MPa (42)] has a fabric corresponding to type-A, having $V_{SV} > V_{SH}$ anisotropy beneath mid-ocean ridges (44). Therefore, the boundary between type-A and type-C or type-D fabric must be $C_{OH} > 800$ ppm H/Si at $\sigma = 1$ to 10 MPa. Consequently, the boundary between type-C (or type-B) and type-A fabric must have a negative slope on this diagram. Such geometry of boundary is consistent with a microscopic model of plastic deformation involving motion of dislocations over a high Peierls barrier (45).

26. J. R. Möckel, *Leidse Geol. Med.* **42**, 61 (1969).

27. K. Frese, V. Trommsdorf, H.-R. Wenk, K. Kunze, *Deform. Mech. Rheol. Tectonics* **53**, 54 (2001).

28. G. Yoshino, *J. Sci. Hiroshima Univ. Ser. C* **3**, 343 (1961).

29. A. L. Littlejohn, H. J. Greenwood, *Can. J. Earth Sci.* **11**, 1288 (1974).

30. J.-G. Schilling, M. B. Bergeron, R. Evans, *Philos. Trans. R. Soc. London Ser. A* **297**, 147 (1980); D. H. Green, T. J. Falloon in *The Earth's Mantle*, I. Jackson, Ed. (Cambridge Univ. Press, Cambridge, 1998), p. 311.

31. D. R. Bell, G. R. Rossman, *Science* **255**, 1391 (1992).

32. S. Karato, *Nature* **319**, 309 (1986).

33. G. Hirth, D. L. Kohlstedt, *Earth Planet. Sci. Lett.* **144**, 93 (1996).

34. S. Karato, H. Jung, *Earth Planet. Sci. Lett.* **157**, 193 (1998).

35. M. S. Paterson, *Bull. Mineral.* **105**, 20 (1982).

36. S. Karato, K.-H. Lee, *Proc. 12th Int. Conf. Texture Mater.* (1999), p. 1546.

37. S. Karato, H. Jung, *Philos. Mag. Ser. A.*, in press.

38. M. Bystricky, K. Kunze, L. Burlini, J.-P. Burg, *Science* **290**, 1564 (2000).

39. S. Zhang, S. Karato, J. D. Fitz Gerald, U. H. Faul, Y. Zhou, *Tectonophysics* **316**, 133 (2000).

40. N. L. Carter, H. G. Avé Lallemant, *Geol. Soc. Am. Bull.* **81**, 2181 (1970).

41. J.-P. Montagner, H.-C. Nataf, *J. Geophys. Res.* **91**, 511 (1986).

42. J.-C. C. Mercier, *J. Geophys. Res.* **85**, 6293 (1980).

43. D. Jin, S. Karato, M. Obata, *J. Struct. Geol.* **20**, 195 (1998).

44. H.-C. Nataf, I. Nakanishi, D. L. Anderson, *J. Geophys. Res.* **91**, 7261 (1986).

45. H. J. Frost, M. F. Ashby, *Deformation Mechanism Maps* (Pergamon, Oxford, 1982), p. 167.

46. We thank K. Fischer, K. Frese, Z. Jiang, J.-P. Montagner, J. Park, and D. Wiens for discussion and K.-H. Lee for technical assistance. T. Hiraga performed the TEM study. Supported by NSF grants EAR-990387 and 0001955 (S.-i.K.) and by the University of Minnesota graduate school Doctoral Dissertation scholarship (H.J.).

3 May 2001; accepted 18 July 2001

Repeating Deep Earthquakes: Evidence for Fault Reactivation at Great Depth

Douglas A. Wiens and Nathaniel O. Snider

We have identified three groups of deep earthquakes showing nearly identical waveforms in the Tonga slab. Relocation with a cross-correlation method shows that each cluster is composed of 10 to 30 earthquakes along a plane 10 to 30 kilometers in length. Some of the earthquakes are collocated, demonstrating repeated rupture of the same fault, and one pair of events shows identical rupture complexity, suggesting that the temporal and spatial rupture pattern was repeated. Recurrence intervals show an inverse time distribution, indicating a strong temporal control over fault reactivation. Runaway thermal shear instabilities may explain temporally clustered earthquakes with similar waveforms located along slip zones weakened by shear heating. Earthquake doublets that occur within a few hours are consistent with events recurring before the thermal energy of the initial rupture can diffuse away.

Earthquakes with highly similar waveforms result when ruptures with identical focal mechanisms are located so close that complexly scattered waves show little difference between events (1). Similar earthquakes at shallow depths have been located accurately by cross-correlation techniques, thus allowing delineation of small features in the seismicity data (2) as well as detailed studies of earthquake recurrence and rupture properties (3, 4). Similar deep earthquakes, although noted previously (5), have not been studied with modern methods. The study of possible repeating deep earthquakes may help to ex-

plain the mechanism that causes seismic rupture at depths of greater than 100 km (6-10).

Using regional broadband waveforms recorded by a 2-year seismograph deployment in 1993-95 (11), we identified three clusters of similar earthquakes in the deep Tonga slab. Seismograms from each cluster show nearly identical waveforms (Fig. 1), suggesting that the earthquakes must have similar focal mechanisms and locations. We used a cross-correlation technique to determine the relative arrival times of the regional P and S waves, as well as teleseismic P phases. The arrival times were then solved for the relative centroid positions and times of the events with a hypocentroidal decomposition method (12). The resulting arrival times and earth-

Department of Earth and Planetary Sciences, Washington University, St. Louis, MO 63130, USA.